A Coded Excitation Framework for High SNR Transcranial Ultrasound Imaging

Emelina P. Vienneau, *Graduate Student Member, IEEE*, and Brett C. Byram, *Member, IEEE*

***Abstract*— Robust transcranial ultrasound imaging is difficult due to poor image quality. In particular, low signal-to-noise ratio (SNR) limits sensitivity to blood flow and has hindered clinical translation of transcranial functional ultrasound neuroimaging thus far. In this work, we present a coded excitation framework to increase SNR in transcranial ultrasound without negatively impacting frame rate or image quality. We applied this coded excitation framework in phantom imaging and showed SNR gains as large as 24.78 dB and signal-to-clutter ratio gains as high as 10.66 dB with a 65 bit code. We also analyzed how imaging sequence parameters can impact image quality and showed how coded excitation sequences can be designed to maximize image quality for a given application. In particular, we show that considering the number of active transmit elements and the transmit voltage is critical for coded excitation with long codes. Finally, we applied our coded excitation technique in transcranial imaging of ten adult subjects and showed an average SNR gain of 17.91 ± 0.96 dB without a significant increase in clutter using a 65 bit code. We also performed transcranial power Doppler imaging in three adult subjects and showed contrast and contrast-to-noise ratio improvements of 27.32 ± 8.08 dB and 7.25 ± 1.61 dB, respectively with a 65 bit code. These results show that transcranial functional ultrasound neuroimaging may be possible using coded excitation.**

***Index Terms*— Coded excitation, transcranial ultrasound imaging, power Doppler imaging, signal-to-noise ratio, image quality.**

I. Introduction

TRANSCRANIAL functional ultrasound neuroimaging is highly challenging due to poor image quality [1], [2], [3], [4], [5]. The high acoustic impedance mismatch between the skull and surrounding tissue as well as its inhomogeneities lead to attenuation and other sources of image degradation that lower the signal-to-noise ratio (SNR) [6]. The high attenuation of the skull also necessitates using a low imaging frequency which further impedes blood flow imaging [7]. The low imaging frequency reduces blood echogenicity and increases the minimum detectable velocity, thereby reducing sensitivity to the slow flow in the microvasculature that is critical to the hemodynamic response [8], [9], [10], [11]. While microbubble contrast agents have been employed to increase SNR in transcranial imaging, due to the long scan times required for microbubble localization, visualizing transient changes in blood flow from the hemodynamic response is difficult. As such, this approach is better suited for angiography rather than functional neuroimaging [12]. Additionally, relying on perfectly timed injections of contrast agents increases complexity and invasiveness and ultimately limits clinical applications. In summary, low SNR has prevented clinical translation of transcranial functional ultrasound neuroimaging thus far.

Coded excitation is a signal processing technique that can increase SNR within FDA safety limits without requiring contrast agents. To perform coded excitation imaging, the transmitted excitation pulse is modulated to increase its time-bandwidth product ($T \cdot BW$) and the received backscattered echoes are then demodulated to recover the original pulse shape and increase the signal amplitude. The demodulation step, also known as pulse compression, is typically performed with a matched filter, resulting in an SNR gain proportional to $10\log_{10}(T \cdot BW)$. Unfortunately, the matched filtering step also introduces range lobes which are bright artifacts in the range (axial) dimension that reduce the effective dynamic range. A coded excitation framework must be designed to balance such factors based on the application [13], [14]. For the challenge of transcranial blood flow imaging, large SNR gains are needed to overcome the degradation caused by the skull and increase the separation between noise and slow blood flow. High dynamic range and a high frame rate are also critical to maintain sensitivity to the blood signal. The ultrasound scanner available for use may also place considerable constraints on the approach.

Frequency modulated signals such as linear instantaneous frequency chirps have been a popular choice in ultrasound imaging due to the large SNR gains they can provide [14], [15], [16]. However, efficient implementation that results in high SNR gains and low range lobe levels requires a multi-state pulser which is unavailable on most systems. In comparison, phase modulation can be implemented with a tri-state or bi-state pulser, making it simpler to

Manuscript received 2 March 2023; accepted 11 April 2023. Date of publication 20 April 2023; date of current version 2 October 2023. The work of Emelina P. Vienneau was supported in part by the National Science Foundation Graduate Research Fellowship Program under Grant 1937963 and in part by the National Institute of Biomedical Imaging and Bioengineering under Grant T32EB021937. The work of Brett C. Byram was supported in part by the National Institute of Biomedical Imaging and Bioengineering under Grant R01EB020040; in part by the National Heart, Lung, and Blood Institute under Grant R01HL156034; and in part by the National Science Foundation CAREER Award under Grant IIS-1750994. *(Corresponding author: Emelina P. Vienneau.)*

This work involved human subjects or animals in its research. Approval of all ethical and experimental procedures and protocols was granted by the Institutional Review Board of Vanderbilt University under Approval No. 180029.

The authors are with the Department of Biomedical Engineering, Vanderbilt University, Nashville, TN 37235 USA (e-mail: emelina.p.vienneau@vanderbilt.edu; brett.c.byram@vanderbilt.edu).

This article has supplementary downloadable material available at https://doi.org/10.1109/TMI.2023.3269022, provided by the authors.

Digital Object Identifier 10.1109/TMI.2023.3269022

implement and more broadly applicable [17], [18], [19], [20]. Phase modulation can be implemented within one transmit-receive event or within multiple events using complimentary sequences such as Golay codes. While complimentary sequences have perfect range lobe supression when no motion is present between complimentary frames, the reduction in frame rate and high sensitivity to motion make this approach less practical for *in vivo* blood flow imaging.

Single-transmit phase encoding schemes such as Barker coded excitation can be implemented on any scanner, do not reduce frame rate, and are less sensitive to motion. Furthermore, Barker codes longer than 2 bits have no spectral nulls so stable inverse filters can be designed for pulse compression with near-perfect range lobe suppression [18], [19], [20], [21]. The loss in SNR gain from inverse filtering instead of matched filtering is generally less than 1 dB, an acceptable tradeoff [22]. However, the longest Barker code is only 13 bits, limiting the maximum achievable SNR gain to only 11 dB.

To solve this dilemma, we have shown that compound Barker codes with full spectral support can be formed by taking the Kronecker product of two or more Barker codes, providing much larger SNR gains still with excellent range lobe suppression [23], [24], [25]. This approach allows for the design of arbitrarily long binary invertible sequences that can produce large SNR gains. Moreover, these SNR improvements can be achieved without sacrificing frame rate or other aspects of image quality and without complex hardware.

Herein, we extend our findings to any binary, invertible, skew-symmetric sequence and describe implementation strategies to achieve best results with the Verasonics Vantage system. Using phantom experiments we provide a detailed analysis of how imaging sequence parameters impact image quality with coded excitation and make recommendations for how to maximize image quality for a given system and application. Finally, we applied our coded excitation framework to transcranial B-Mode imaging in ten adult volunteers and transcranial power Doppler imaging in three adult volunteers.

II. Coded Excitation Framework

A. The Binary Sequence

The coded excitation waveform is formed by convolving a base pulse with an upsampled binary sequence of $+1$'s and -1's which represent $0°$ and $180°$ phase shifts, respectively. The choice of binary sequence is critical for several reasons. First, in order to use an inverse filtering approach for pulse compression (see Section II-D), the binary sequence must be invertible, meaning that there are no zeros in the Fourier domain [17], [18], [19], [20]. All Barker codes longer than 2 bits are invertible. Maximum-length sequences (m-sequences) are also invertible and others have been discovered as well [22].

Another requirement of the binary code, c, is that it is of odd length and skew-symmetric, i.e., it obeys the following:

$$c(N'-l) = (-1)^l c(N'+l),\ 0 \le l \le N', \tag{1}$$

where $2N'+1$ is equal to the total length of the code, N. All of the odd-length Barker codes are skew-symmetric. In addition to Barker codes, there are other invertible binary codes such as the 3-bit m-sequence that are also skew-symmetric [17], [22]. Skew-symmetry is required due to the manner in which the decoding filter is constructed. In particular, it is because of the use of the chip waveform that the binary code must be skew-symmetric; without the chip waveform, this no longer is a requirement. See Section II-D for more details.

Next, since SNR gain depends on the code length and is proportional to $10\log_{10}(N)$, it is desirable to create long binary codes that are also invertible and skew-symmetric. Long sequences can be obtained from shorter ones (such as Barker codes) via the Kronecker product which is defined by:

$$\mathbf{a} \otimes \mathbf{b} = (a_1\mathbf{b}, a_2\mathbf{b}, a_3\mathbf{b}, \ldots, a_{N_a}\mathbf{b}). \tag{2}$$

If sequence $\mathbf{a} = (a_1, a_2, \ldots, a_{N_a})$ is of length N_a and sequence $\mathbf{b} = (b_1, b_2, \ldots, b_{N_b})$ is of length N_b, the Kronecker product will be of length $N_a \times N_b$ [26]. The Kronecker product of two invertible, skew-symmetric sequences will also be invertible and skew-symmetric [22]. In this way, arbitrarily long codes can be created by computing the Kronecker product of an arbitrary number of shorter codes. An example of a compound code and its Fourier transform is shown in Fig. 1.

Finally, sequences with low noise enhancement factors are needed to minimize the loss in SNR gain when pulse compression is performed with an inverse filter instead of a matched filter (see Section II-D). The noise enhancement factor is related to the spectral properties of the binary code. An exhaustive search for optimal binary, invertible, skew-symmetric sequences with the lowest noise enhancement factors has been performed for codes up to 32 bits by Ruprecht & Rupf [22]. Since the noise enhancement factor of a Kronecker product sequence can be approximated by the sum of the noise enhancement factors of the constituent sequences, this approach has been used to generate longer, near-optimal sequences [22].

B. The Encoding Chip Waveform

The chip waveform is an application-dependent pulse that defines the axial resolution of the system and fits within the bandwidth of the ultrasound transducer (*e.g.*, a single-cycle sine wave at the transducer center frequency). However, many ultrasound scanners have a tri-state pulser, meaning that they can only produce voltage signals at positive rail voltage, zero voltage, and negative rail voltage. As such, a sinusoid cannot be transmitted directly so a tri-state representation of that pulse is used instead. This tri-state pulse is referred to as the "encoding chip" because it is the chip waveform that is used to create the coded excitation waveform. The length of the encoding chip directly influences the bandwidth of the transmitted pulse and is an important design consideration for maximal transmission efficiency [27].

C. Formation of the Coded Excitation Waveform

To create the coded excitation waveform, the encoding chip and the binary code are convolved. If the binary code were transmitted directly, most of the energy content would be outside the passband, resulting in inefficiency and heating of the transducer. Before convolution, the binary sequence must be upsampled by a factor of $T_p f_s$, where T_p is the spacing of

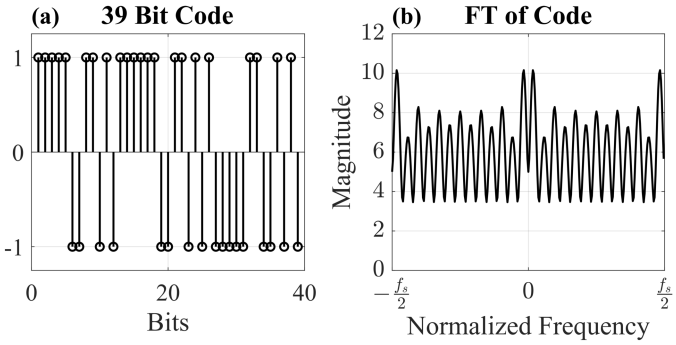

Fig. 1. **(a)** 39 bit binary, invertible, skew-symmetric code. This code was formed by taking the Kronecker product of the 3 bit and 13 bit Barker codes. **(b)** The magnitude of the Fourier transform of the binary code shown in **(a)**. The spectrum never crosses zero, indicating that this binary code is invertible.

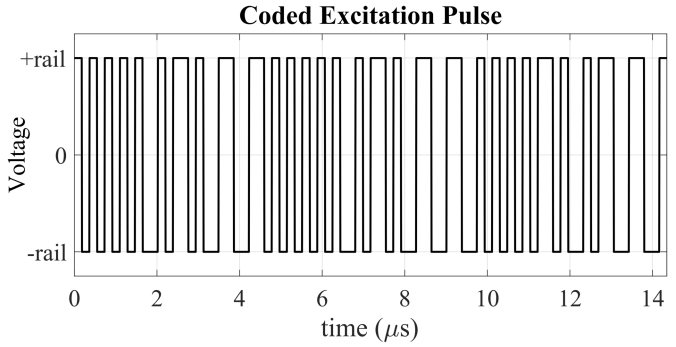

Fig. 2. The tri-state voltage coded excitation waveform generated by upsampling the 39 bit code in Fig. 1a and convolving it with a tri-state representation of a single-cycle sine wave at 2.7174 MHz. Note that the code was upsampled by a factor equal to the length of the encoding chip. The result is a coded excitation pulse with no instances of zero voltage, only $\pm$ rail voltage.

the chip waveforms in the coded excitation pulse and f_s is the axial sampling frequency. This coded excitation signal, $x(n)$, is given by

$$x(n) = \sum_{l=0}^{N-1} c(l)\, p(n - l T_p f_s), \tag{3}$$

where N is the length of the binary code c and p is the encoding chip waveform [19], [20]. Best results are obtained when T_p is exactly equal to the encoding chip duration. An example coded excitation waveform is shown in Fig. 2 where the 39 bit binary code shown in Fig. 1a was upsampled and convolved with tri-state representation of a single-cycle sine wave at 2.7174 MHz. Note that T_p is exactly equal to the duration of the encoding chip and there are no zero voltage states in the coded excitation pulse. To create such a coded excitation waveform on the Verasonics, we used the 'pulseCode' waveform type instead of the 'parametric' waveform type. By directly supplying the pulse code which describes the sequence of tri-level voltage states, we did not have to use the arbitrary waveform generator. Finally, note that there are no equalization pulses at the beginning or end as found with 'parametric' waveforms.

In summary, combining multiple binary, invertible, skew-symmetric sequences with the Kronecker product to create arbitrarily long sequences offers the opportunity to achieve dramatic improvements in SNR without complex hardware, a reduction in frame rate, or a reduction in image quality.

D. Construction of the Decoding Filter

The second key aspect to this coded excitation framework is the design of a decoding filter for pulse compression that simultaneously achieves near-perfect range lobe suppression while still providing a very large SNR gain. This can be achieved by constructing a decoding filter that serves as an inverse filter for the binary sequence and a matched filter for the chip waveform, providing an SNR gain of $10\log_{10}(N) - \epsilon$ when compared to simply transmitting the chip waveform and processing it with a matched filter. The term ϵ is the noise enhancement factor (discussed in Section II-A) that represents the loss in SNR gain from inverse filtering instead of matched filtering. However, comparing the SNR gain to a non-coded transmit without matched filtering yields an even higher gain.

The decoding filter used for pulse compression can be described as an L-tap finite impulse response (FIR) pseudo-inverse filter, where "pseudo" refers to the fact that the filter approximates the inverse spectrum of the code with a truncated Fourier series. In other words, the first L samples of the inverse discrete Fourier transform of the binary code are used to construct the decoding filter. The first step to creating the decoding filter is therefore to compute the discrete-time Fourier transform of the binary code. Note that this is not performed on the upsampled binary code nor is it performed on the coded excitation pulse (i.e., the chip convolved with the upsampled code). Using a Fourier matrix, the M-point Fourier transform, $C(f)$, of a binary code c of length N is given by

$$C(f) = \frac{1}{N} \sum_{n=0}^{N-1} c(n) \mathrm{e}^{-j2\pi(f/f_s)n}, \quad -\frac{f_s}{2} \leq f < \frac{f_s}{2}, \tag{4}$$

where the frequency f has M evenly spaced samples between the provided bounds and f_s is the axial sampling frequency. To evaluate (4), the $M \times N$ Fourier matrix, $\mathrm{e}^{-j2\pi(f/f_s)n}$, is formed and subsequently multiplied by the $N \times 1$ binary code, $c(n)$, via a matrix multiplication operation, resulting in an $M \times 1$ spectrum, $C(f)$. The resulting spectrum is then inverted and centering phase shifts are applied as follows in (5),

$$D(f) = \frac{1}{C(f)} \frac{\mathrm{e}^{-j\pi(f/f_s)(L-1)}}{\mathrm{e}^{j\pi(f/f_s)N}}, \tag{5}$$

where L is the desired number of filter taps and f is defined as in (4) [19] and [20]. This direct inversion is stable specifically because the binary code is invertible. Note that $M \geq L > N$ [20]. To compute the first L FIR filter coefficients in the time domain, the $L \times M$ Fourier matrix, $\mathrm{e}^{j2\pi(lm/M)}$, must be multiplied by the spectrum $D(f)$ in (5) [19] and [20]. This inverse filter, $h(l)$, is given by

$$h(l) = \frac{1}{M} \sum_{m=0}^{M-1} D(f) \mathrm{e}^{j2\pi(lm/M)}, \quad l \in [0, L-1], \ m \in [0, M-1]. \tag{6}$$

Finally, the convolution with the chip waveform must be taken into account by upsampling $h(l)$ in (6) by a factor of $T_p f_s$ and

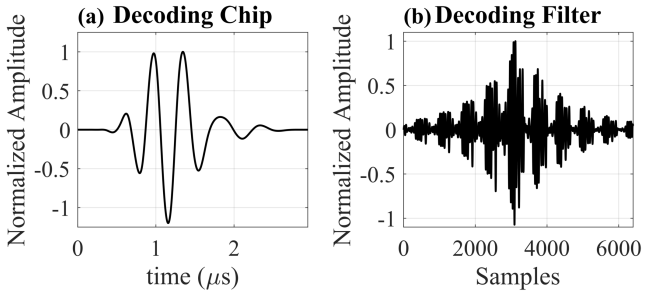

Fig. 3. **(a)** An impulse response for the P4-2v transducer at 2.7174 MHz from Verasonics Simulate Mode. This waveform should be used to form the decoding filter. Note that the decoding chip is longer than the encoding chip, but the variable T_p is still set based on the encoding waveform duration. Also note that this waveform shown here was resampled at a higher frequency than used for decoding for display purposes. **(b)** The 128-tap decoding filter constructed using the decoding chip shown in **(a)**.

convolving it with the time-reversed chip waveform, p. The final decoding filter, $g(n)$, is given by (7) [19] and [20].

$$g(n) = \sum_{l=0}^{L-1} h(l)\, p(-n + l T_p f_s) \tag{7}$$

This filter serves as an inverse filter for the binary code and a matched filter for the chip, effectively performing complete code compression and range lobe suppression.

Note that this is not the same as filtering with (6) and then performing matched filtering. In order to temporally align the chip pulse repetitions and completely suppress range lobes, the upsampling of the decoding filter as shown in (7) must be included. The convolution with the chip pulse is optional but recommended to increase the SNR gain.

In Section II-A it was mentioned that the binary code needs to be skew-symmetric. It is the upsampling in (7) that specifically requires this. If the binary code were transmitted directly without first upsampling it and convolving it with a chip waveform (as is common in communications applications), then (6) would suffice for decoding as opposed to (7), meaning that non-skew-symmetric binary invertible sequences could be used as well. However, in ultrasound imaging the bandwidth of the transducer must be taken into account by using the encoding chip instead of directly transmitting the code.

E. Decoding Chip Waveform

In reality, the impulse response of an ultrasound transducer differs from the idealized tri-state voltage signal that is used to excite the transducer. A realistic transducer impulse response has a finite bandwidth and usually includes ring-down. The chip used to construct the decoding filter (the "decoding chip") should therefore take this impulse response into account. Although the duration of the transducer impulse response is generally longer than the excitation voltage signal, it is important that the variable T_p in (7) is still set to the exact length of the encoding chip and not the length of the impulse response. For use in (7), the decoding chip must be sampled at the same frequency, f_s.

The decoding chip can be determined by a measured or simulated one-way or two-way impulse response of the system. The one-way impulse response can be measured with a hydrophone in a water tank or obtained from the transducer specifications (if available). The two-way impulse response can be measured with the imaging system and a perfectly reflecting point target or it could be approximated with a simulation such as the Verasonics Simulate Mode. We compared an impulse response measured by the hydrophone at a 2.7174 MHz transmit frequency, the impulse response printed on our transducer's data sheet, and an impulse response from Verasonics Simulate Mode in which we simulated imaging of a point target at a transmit focus of 10 cm with a 2.7174 MHz transmit frequency. We also tested using a delta function of the appropriate length for the decoding chip. While all of these decoding chips produced reasonable results, the Verasonics Simulate Mode decoding chip produced the lowest range lobe levels and the largest SNR gains. This could be because it is a two-way impulse response and is therefore the best model of the system. This decoding chip and the resulting 128-tap decoding filter are shown in Fig. 3.

F. Pulse Compression

The decoding filter derived in Section II-D is applied via convolution along the axial dimension. We sampled the decoding filter at $4f_0$, the axial sampling frequency of the data acquired on the Verasonics. Decoding can be performed on the channel data prior to beamforming or it can be applied after delaying and summing across channels but prior to envelope detection. The advantage of performing decoding on the beamformed data is the reduced computational cost, but beamforming first can introduce pulse distortions from the time delays that degrade code compression, particularly in the nearfield. We performed decoding on the channel data since our goal was to optimize image quality and do offline postprocessing. In the future, a GPU implementation for decoding of channel data and/or beamformed data would be highly beneficial for increasing the computational speed for real-time application.

Finally, time gain compensation (TGC) must be accounted for with longer codes. If the TGC profile is changing rapidly, long codes will experience a different gain profile throughout their spatial extent, effectively creating an amplitude modulation and reducing pulse compression efficacy. To account for this, we divided the channel data by the gain at each depth before pulse compression. After pulse compression, we multiplied by the gain profile to restore the image brightness.

G. Code Availability

Example code demonstrating implementation of this coded excitation framework in MATLAB is provided here: https://github.com/VU-BEAM-Lab/CodedExcitation. Functions to generate compound codes and decoding filters, perform pulse compression, and generate the pulse code for programming the Verasonics are provided.

III. Methods

A. Physical Phantom Imaging

Imaging of a general purpose phantom (Model 054GS, CIRS, Inc., Norfolk, VA, USA) was performed with a

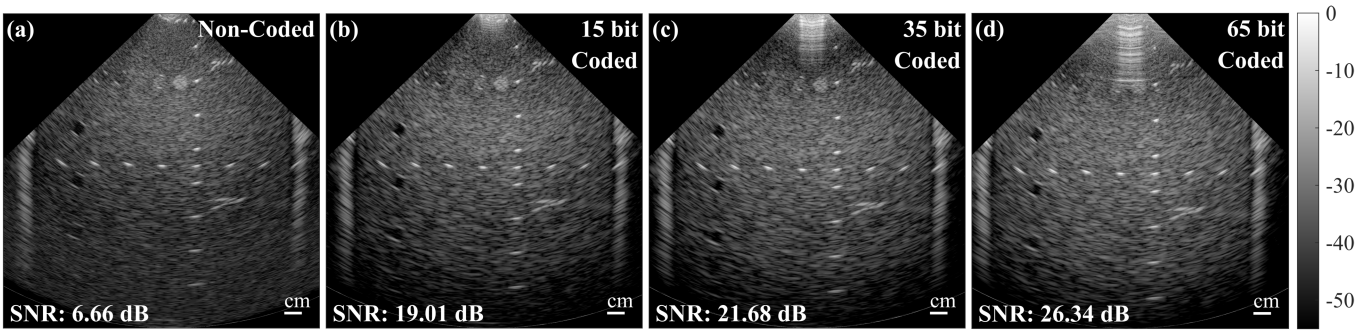

Fig. 4. Comparison of non-coded and coded excitation focused B-Mode image acquisition in a general purpose CIRS phantom. The transmit voltage was 11 V and the entire aperture was used for transmit. **(a)** Non-coded excitation. **(b)** 15 bit coded excitation. **(c)** 35 bit coded excitation. **(d)** 65 bit coded excitation.

TABLE I
VARIABLE PARAMETERS FOR PHANTOM EXPERIMENT 1

Parameter	Value
Transmit voltage (V)	11, 41
Transmit elements	8, 16, 24, 32, 40, 48, 56, 64
Code length	3, 5, 7, 11, 13, 15, 25, 35, 45, 55, 65, 75

TABLE II
VARIABLE PARAMETERS FOR PHANTOM EXPERIMENT 2

Parameter	Value
Transmit voltage (V)	6, 11, 16, 21, 26, 31, 36, 41
Transmit elements	15, 32, 64
Code length	13, 39, 65

P4-2v phased array (64 elements, 0.3 mm pitch, 64.4% bandwidth) operating at 2.7174 MHz and a Verasonics Vantage 128 scanner (Verasonics, Kirkland, WA, USA). The extended transmit option on the Verasonics was used. The probe was fixed in a probe holder to minimize motion. Focused B-Mode and focused M-Mode imaging sequences as described in Section III-C were used. Imaging was conducted with non-coded and coded transmits of varying code lengths to analyze SNR gain and signal-to-clutter ratio (SCR) gain as a function of code length (see Section III-D). Two phantom experiments were conducted with the imaging parameters in Tables I and II. All of the compound codes were formed from Barker codes. All of the data for each experiment were acquired without moving the transducer. See Appendix A for acoustic output measurements corresponding to the imaging sequence and parameter combinations shown in Tables I and II.

B. In Vivo Transcranial Imaging

Transcranial imaging was performed with a P4-2v phased array operating at 2.7174 MHz and a Verasonics scanner. Acoustic output was measured with a hydrophone to ensure it was within FDA limits (see Appendix A) [28]. All imaging was done in accordance with a protocol approved by the local IRB. Imaging was performed at the right temporal acoustic window in the transverse plane. The transducer was hand-held and positioned such that the midbrain was clearly visible on B-Mode imaging. The basal cerebral arteries that surround the midbrain were captured with power Doppler imaging.

To measure SNR gain, ten healthy adult volunteers were scanned (age range 24-55, mean $\pm$ standard deviation age 36 ± 13; three female and seven male; six White, three Asian, one Hispanic). Focused B-Mode imaging and focused M-Mode imaging with and without coded excitation were each performed in immediate succession to match field-of-views (see Section III-C). Data were acquired with 13, 25, 39, and 65 bit codes at 21 V using all transmit elements. The voltage was chosen based on results from the phantom study discussed in Section IV-B and IV-C. The M-Mode data were used to calculate SNR and SCR (see Section III-D).

To demonstrate improvements in blood flow imaging, three different adult volunteers (age range 23-26; two males and one female; White) were scanned with a diverging wave synthetic aperture power Doppler sequence (see Section III-C) with and without coded excitation. Code lengths of 13, 39, and 65 bits and transmit voltages of 6 V and 21 V were used. The value of 21 V was chosen based on the phantom study as mentioned previously and 6 V was additionally investigated as a low signal case to emulate an "insufficient" acoustic window. Contrast-to-noise ratio (CNR) and contrast ratio (CR) were computed for non-coded and coded excitation power Doppler images. Focused M-Mode data were also acquired in these volunteers to calculate SNR.

C. Imaging Sequences and Beamforming

For all imaging sequences, the non-coded excitation transmit waveform was a single-cycle parametrically defined pulse at a center frequency of 2.7174 MHz with a bandwidth of 1.45 MHz. The tri-state representation of this waveform was the encoding chip for the coded excitation transmit waveforms which were created according to Section II-C with various code lengths. Delay-and-sum with dynamic receive beamforming was used. Regardless of how many elements were used for transmit, all 64 elements received data and were used for beamforming. Pulse compression was applied on the channel data as described in Section II-F. The 256-tap decoding filter was constructed according to Sections II-D and II-E.

1) Focused B-Mode: The scan geometry was a 90° sector with 129 evenly spaced beams. The focal depth was 8 cm for the phantom imaging and 10 cm for the *in vivo* imaging. The imaging depth was 16 cm and two frames were acquired.

2) Focused M-Mode: The imaging parameters for the focused M-Mode sequence were the same as the focused B-Mode sequence described in Section III-C.1 except that

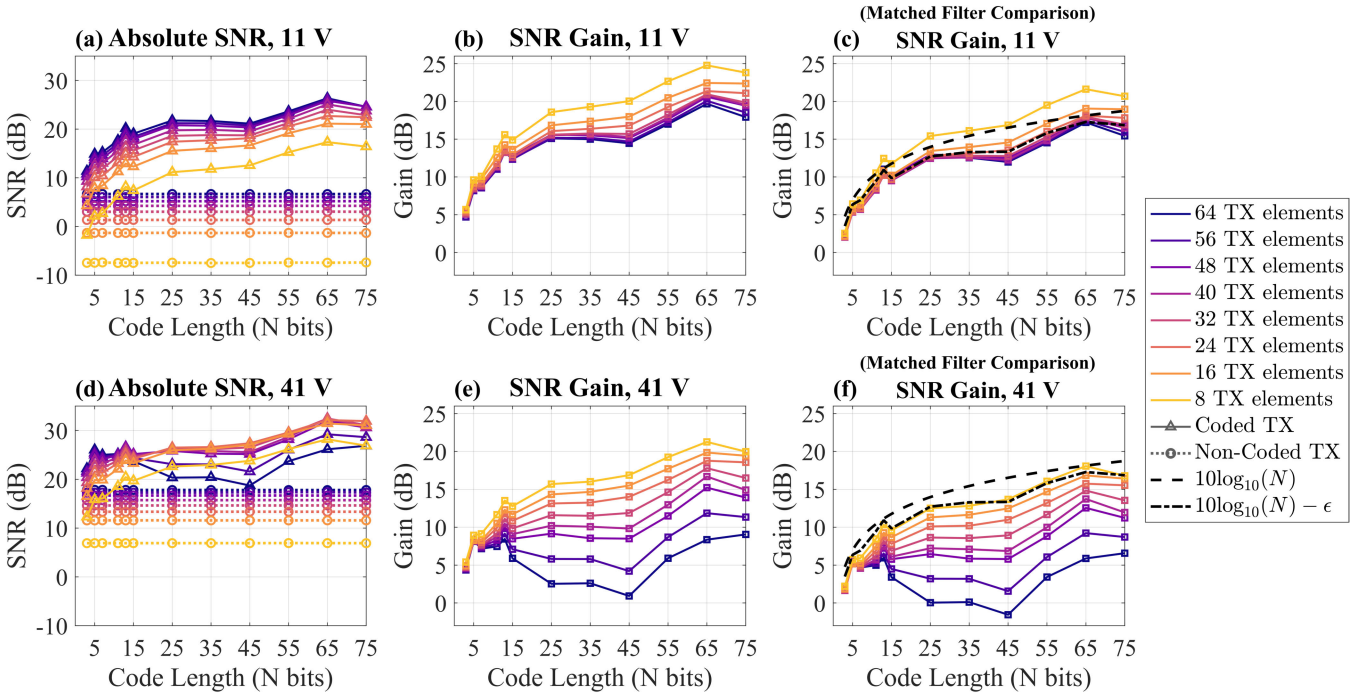

Fig. 5. SNR and SNR gain as a function of code length for 11 V and 41 V transmits. TX = transmit. **(a)** Absolute SNR for coded and non-coded transmits at 11 V. **(b)** SNR gain at 11 V. **(c)** SNR gain at 11 V where the non-coded data were additionally processed with a matched filter. The theoretical SNR gain of $10\log_{10}(N)$ is included for reference with and without the noise enhancement factor (ϵ) taken into account. **(d)** Absolute SNR for coded and non-coded transmits at 41 V. **(e)** SNR gain at 41 V. **(f)** SNR gain at 41 V where the non-coded data were additionally processed with a matched filter. The theoretical SNR gain of $10\log_{10}(N)$ is included for reference with and without the noise enhancement factor (ϵ) taken into account. Note that error bars are not shown because they would not be visible; the SNR standard deviation values were all less than 0.4 dB.

instead of 129 beams spanning 90°, 2000 beams were acquired with a steering angle of 0° to obtain data with a high frame rate or pulse repetition frequency (PRF) of 1 kHz.

3) Diverging Wave Synthetic Aperture Power Doppler: The diverging wave synthetic aperture (DWSA) power Doppler sequence used 8 diverging wave transmits with 15 element sub-apertures for each acquisition. There were 1100 acquisitions with a 550 Hz frame rate. For beamforming, a sector geometry with a 90° opening angle and a radius of 9.6 mm was chosen and 128 evenly spaced beams were beamformed. Singular value decomposition (SVD) was used to filter clutter and noise [29].

D. Image Quality Metrics

To quantify the image quality improvements from coded excitation and analyze imaging parameter tradeoffs, we calculated several image quality metrics from the phantom M-Mode imaging and the *in vivo* transcranial M-Mode imaging. The SNR and SCR were measured using a previously reported spatiotemporal coherence technique [30], [31]. By measuring temporal lag-one coherence across repeated acquisitions and spatial lag-one coherence across the channel dimension, thermal noise and incoherent acoustic clutter can be quantified separately. Additionally, this measure of SNR does not include stationary clutter as part of the "signal" term. This technique is accurate across a wide dynamic range of clinically relevant noise and clutter levels and has been demonstrated in transcranial imaging [30], [31]. Furthermore, this technique is sensitive to spatially incoherent sources of clutter. Since range lobes from imperfect pulse compression are temporally stable but spatially incoherent similar to reverberation, we expect that measuring SCR will be a good indicator of pulse compression efficacy.

SNR and SCR are measured according to (8) and (9), respectively, where P_s is the power of the uncorrupted signal of interest, P_N is the power of the thermal noise, and P_c is the power of the incoherent acoustic clutter (*e.g.*, reverberation).

$$\text{SNR} = 10\log_{10}(P_s/P_N) \tag{8}$$

$$\text{SCR} = 10\log_{10}(P_s/P_c) \tag{9}$$

The M-Mode data were used for these calculations since a high PRF is needed to calculate temporal correlation when motion is present *in vivo*. Spatial and temporal lag-one coherence, which were used to compute P_s, P_c, and P_N, were computed within an ROI centered about the transmit focus. This ROI had a 2 mm axial extent. For additional details on how these metrics are calculated, please see Vienneau et al. [31]. The SNR gain was calculated as $\text{SNR}_{\text{gain}} = \text{SNR}_{\text{coded}} - \text{SNR}_{\text{non-coded}}$ and the SCR gain was calculated as $\text{SCR}_{\text{gain}} = \text{SCR}_{\text{coded}} - \text{SCR}_{\text{non-coded}}$.

IV. Results

A. Coded Excitation Demonstration in a Phantom

A comparison of non-coded and coded excitation B-Mode imaging in a phantom is shown in Fig. 4. SNR increases markedly with increasing code length. The higher SNR in the coded images is most notable at deeper depths where there is more attenuation. In particular, the deeper anechoic cysts are much more apparent. The nearfield artifacts in the longer 35 bit

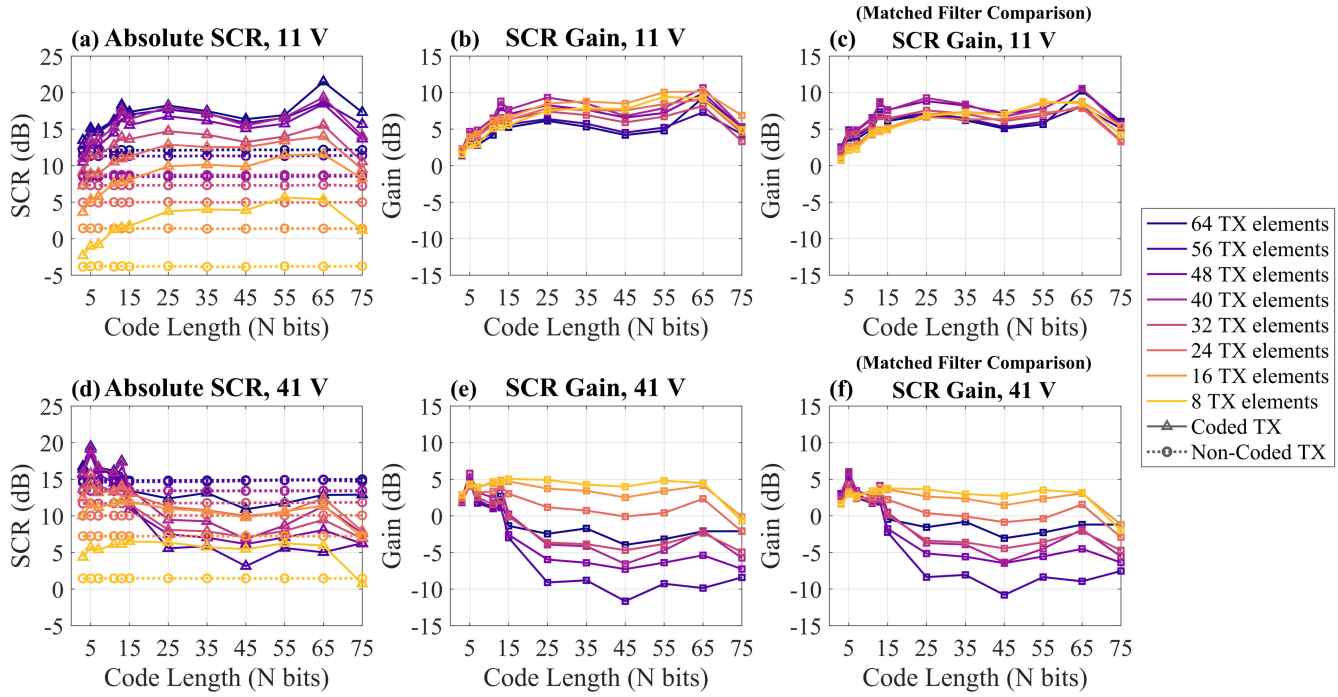

Fig. 6. SCR and SCR gain as a function of code length for 11 V and 41 V transmits. TX = transmit. **(a)** Absolute SCR for coded and non-coded transmits at 11 V. **(b)** SCR gain at 11 V. **(c)** SCR gain at 11 V where the non-coded data were additionally processed with a matched filter. **(d)** Absolute SCR for coded and non-coded transmits at 41 V. **(e)** SCR gain at 41 V. **(f)** SNR gain at 41 V where the non-coded data were additionally processed with a matched filter. Note that error bars are not shown because they would not be visible; the SCR standard deviation values were all less than 0.1 dB.

and 65 bit coded images (Fig. 4c and 4d) are due to receiving data while the coded pulse was still being transmitted. This is also referred to as the dead zone or blind zone.

B. SNR & SCR Analysis for Phantom Experiment 1

Fig. 5a shows that the SNR generally increases with increasing code length as expected. There are a few instances of longer codes producing lower SNR gains, *e.g.*, 15 versus 13 bits. This is because certain codes compress more efficiently with an inverse filter (see Section II-A). For instance, the 13 bit Barker code has a noise enhancement factor of 0.21 dB whereas the 15 bit code has a noise enhancement factor of approximately 1.91 dB [22]. The difference between $10\log_{10}(15)$ and $10\log_{10}(13)$ is only about 0.62 dB which is why the SNR is lower for the 15 bit code versus the 13 bit code.

Fig. 5a also shows that reducing the number of transmit elements reduces the SNR for non-coded and coded data because the acoustic pressure is lower. For reference, the acoustic pressure range based on hydrophone measurements was 0.032 - 0.490 Pa for the 11 V data and 0.200 - 0.963 Pa for the 41 V data (derated by 0.76 dB/MHz/cm). However, the SNR for the non-coded data using 8 and 16 transmit elements is negative which is lower than expected. We suspect that this was due to attenuation from the phantom (approximately 16.52 dB at the focus given our phantom's attenuation coefficient of 0.76 dB/MHz/cm) in combination with low acoustic pressure from using few transmit elements and a low voltage (acoustic pressure was 0.032 Pa for 8 transmit elements and 0.064 Pa for 16 transmit elements).

Comparing Fig. 5a to 5d, it is evident that absolute SNR is generally higher for the 41 V case than the 11 V case as expected. However, in the 11 V case, the highest SNR is achieved using all 64 elements, whereas in the 41 V case, the highest SNR is achieved with approximately half of the elements. One explanation for this is that the pulser may be unable to supply enough power at a high voltage for all transmit elements for longer codes. However, regardless of the transmit voltage, using coded excitation of at least 13 bits and as few as 8 transmit elements still provides a higher absolute SNR than using the full aperture without coded excitation.

While the absolute SNR levels tend to decrease with decreasing number of transmit elements (Fig. 5a and 5d), the SNR gain increases (Fig. 5b and 5e). SNR gain also increases with lower transmit voltage. Furthermore, the spread between SNR gain measurements across number of transmit elements becomes wider with longer codes versus shorter codes and with higher transmit voltage (Fig. 5e) versus lower transmit voltage (Fig. 5b). We hypothesize that this is due to system transmit nonlinearities that worsen with the increased demand on the system when using more transmit elements, longer codes, and higher voltages. Such nonlinearities lead to imperfect pulse compression which contributes to the appearance of range lobes and the loss in SNR gain. This shows that number of transmit elements and transmit voltage are important considerations for coded excitation with longer codes. Ultimately, the largest SNR gain of 24.78 dB occurs with an 11 V transmit voltage, 8 transmit elements, and a 65 bit code (Fig. 5b).

Figs. 5c and 5f show the SNR gain in which the non-coded excitation data were additionally processed with a matched filter. In this case, the SNR gain should follow

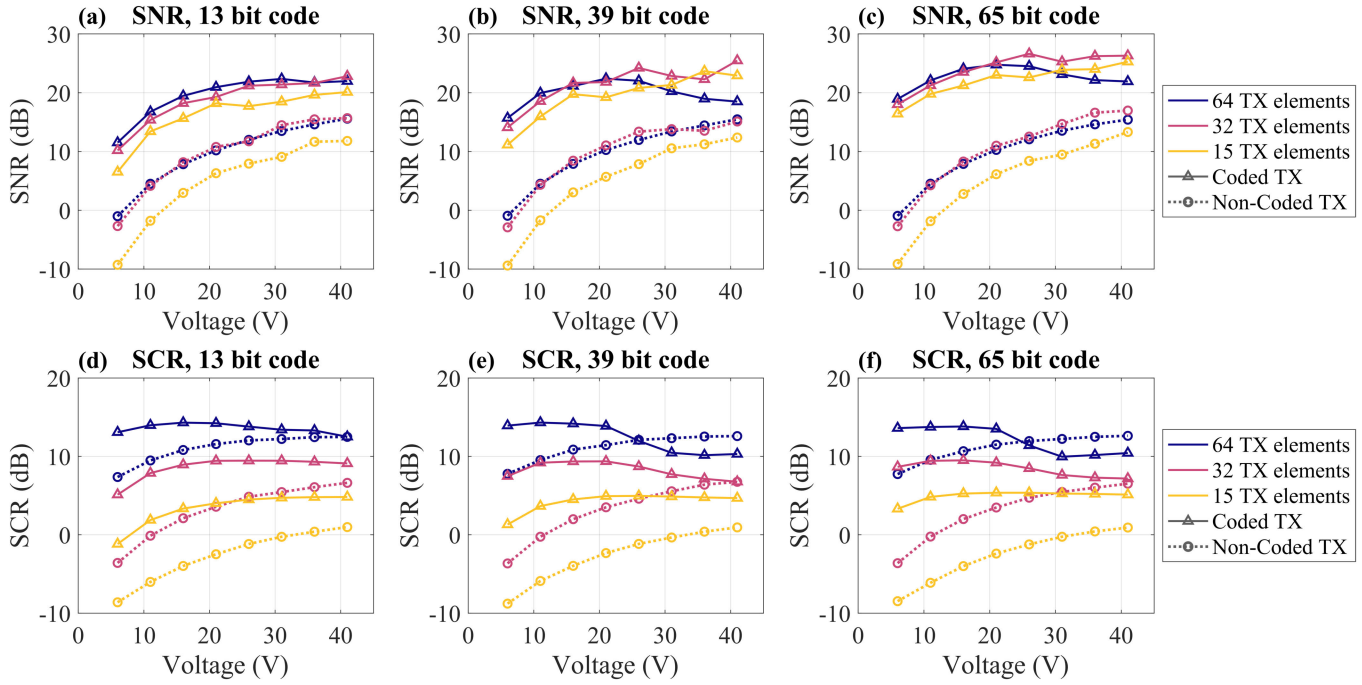

Fig. 7. SNR and SCR as a function of transmit voltage for non-coded and coded excitation transmits with varying code lengths (indicated in the titles) and varying numbers of active transmit elements (indicated in the legends). TX = transmit. **(a)** SNR for non-coded and 13 bit coded excitation. **(b)** SNR for non-coded and 39 bit coded excitation. **(c)** SNR for non-coded and 65 bit coded excitation. **(d)** SCR for non-coded and 13 bit coded excitation. **(e)** SCR for non-coded and 39 bit coded excitation. **(f)** SCR for non-coded and 65 bit coded excitation. Note that error bars are not shown because they would not be visible.

$10\log_{10}(N) - \epsilon$ (the theoretical limit). The noise enhancement factors were derived from [22]. In Fig. 5c, The SNR gains for 24 transmit elements and higher follow the theoretical limit very well. For 8 and 16 transmit elements, the SNR gain exceeds the theoretical limit which should not be possible. However, as mentioned previously, the non-coded SNR for 8 and 16 transmit elements was very low (Fig. 5a), possibly leading to an SNR gain being higher than theoretically possible for those two cases. For the 41 V cases in Fig. 5f, this is not an issue and the curves generally stay below the theoretical limit. The exception is the 8 transmit element curve which slightly exceeds the limit in a few cases for the longer compound codes. This is likely because the ϵ values for these compound codes were only approximated from those of their constituent codes. In summary, these results show that with lower transmit voltage (or higher transmit voltage and fewer active transmit elements), the measured SNR gain very closely approximates the theoretical maximum that we could expect to achieve.

We next analyzed SCR levels to determine the impact of coded excitation on clutter levels as shown in Fig. 6. Fig. 6a (11 V) shows that for coded and non-coded excitation, SCR increases with increasing number of transmit elements. This is likely due to a reduction of off-axis clutter that results from using a larger transmit aperture. There are also slight dips in SCR for the 15, 45, and 75 bit codes that compress less efficiently with an inverse filter, indicating that SCR is sensitive to range lobe clutter from imperfect code compression. Similarly, in Fig. 6d (41 V), SCR increases with increasing number of transmit elements for the non-coded cases and is higher overall than SCR of the non-coded cases in Fig. 6a. However, for the coded excitation cases using 15 bit codes and longer, the SCR decreases.

Similarly, SCR gain for the low voltage case (Fig. 6b) is positive for all code lengths and numbers of transmit elements, whereas for the high voltage case (Fig. 6e), SCR gain becomes negative for codes longer than 13 bits using about half of the transmit aperture or more. The maximum SCR gain of 10.66 dB occurs with a 65 bit code, 40 transmit elements, and 11 V. Finally, Figs. 6c and 6f show that calculating SCR gain with the matched filtered non-coded data makes little difference.

From the results shown in Figs. 5 and 6, a few key takeaways are possible. First, although SNR *gain* is highest with a low voltage, low number of transmit elements, and long codes, ultimately the goal is to improve the absolute SNR of our image. With that in mind, the highest SNR is achieved using a higher voltage, mid-range number of transmit elements, and long codes. However, SCR gain becomes negative for high voltages, so ultimately the voltage must be kept to a moderate level to prevent a loss in SCR. In order to shed more light on what voltages would be best to use moving forward for our *in vivo* study, we conducted an additional phantom experiment which is described in Section IV-C.

C. SNR & SCR Analysis for Phantom Experiment 2

Figs. 7a-7c show that the SNR generally increases with voltage for both coded and non-coded excitation as expected. Notable exceptions are the 39 bit and 65 bit coded excitation cases with all 64 transmit elements. In these cases, the SNR increases up until about 21 V and then begins to decrease. We hypothesize that this is due to transmit nonlinearities that worsen with increased pulse length, voltage, and number of transmit elements.

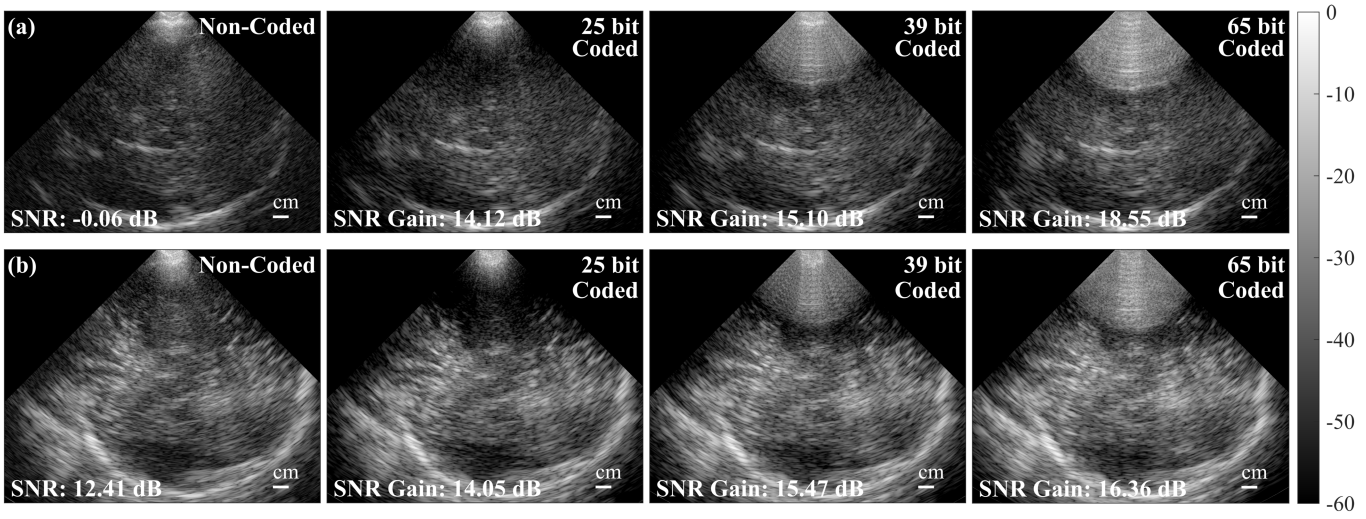

Fig. 8. *In vivo* transcranial B-Mode imaging with and without coded excitation in two subjects. **(a)** Top row: low image quality case (Subject 3, a 50 year old White female). **(b)** Bottom row: high image quality case (Subject 5, a 24 year old White male). In both cases, SNR gain increases with increasing code length. The greatest gain is achieved with the 65 bit code in the low image quality case. The 39 bit and 65 bit codes show the same nearfield artifact from transmitting and receiving at the same time (the dead zone).

Figs. 7d-7f show that SCR increases with voltage for non-coded excitation imaging. However, for the coded excitation imaging, the SCR increases with increasing voltage to a point and then begins to decrease or plateau. The fewer the transmit elements, the greater the benefit of increasing voltage and the greater the SCR gain. Finally, for the 39 bit and 65 bit coded excitation cases with 64 transmit elements, the coded excitation SCR drops below the non-coded excitation SCR beyond about 26 V. For this reason, a transmit voltage of 21 V was used for the *in vivo* imaging discussed in Section IV-D.

Analysis of Fig. 7 demonstrates the utility of assessing SNR and SCR as a function of voltage. There are very clear turning points for SNR and SCR beyond which increasing the voltage any further results in a reduction in image quality rather than an improvement. Furthermore, this analysis can be used to determine a recommended voltage to maximize the SNR (and SCR) for a given imaging sequence.

D. In Vivo Transcranial Imaging

Fig. 8 shows examples of non-coded and coded excitation B-Mode images at 21 V for two subjects: Subject 3, a 50 year old White female representing a low image quality case, and Subject 5, a 24 year old White male representing a high image quality case. High image quality was defined as having a high SNR and SCR. The SNR gain from coded excitation increases with increasing code length as shown qualitatively in the speckle texture and quantitatively with the SNR measurements given in each panel (Fig. 8). In the 39 bit and 65 bit cases, the nearfield artifact from transmitting and receiving at the same time is evident similar to the results in the CIRS phantom (Fig. 4).

The average SNR gains across the 10 subjects for the 13 bit, 25 bit, 39 bit, and 65 bit codes at 21 V were 11.26 ± 0.78 dB, 13.34 ± 0.87 dB, 15.10 ± 1.35 dB, and 17.91 ± 0.96 dB. The average SCR gains were −0.41 ± 0.95 dB, −0.40 ± 0.57 dB, −0.28 ± 1.47 dB, and −0.21 ± 0.76 dB. Overall, the SNR gains were slightly lower than those seen in the CIRS phantom (about 18 dB *in vivo* versus about 24 dB in the phantom with the 65 bit code). There was also a tendency for coded excitation to reduce SCR slightly, although the standard deviation always included 0 dB gain. In comparison, there were moderate increases in SCR of 5-10 dB in the phantom imaging. The presence of the skull in the *in vivo* data likely hindered pulse compression. The heterogeneous structure of the skull and its highly variable acoustic properties lead to sources of image degradation such as reverberation. Severe frequency dependent attenuation through the skull also leads to waveform distortion. All of these effects negatively impact pulse compression, thereby reducing SNR gain and increasing clutter compared to the phantom imaging case.

To further analyze these trends, we conducted linear regressions with SNR, SNR gain, SCR, and SCR gain as the dependent variables and code length as the independent variable. With a significance level of 0.05, we found that code length is a statistically significant predictor of SNR and SNR gain but not of SCR or SCR gain. The F-statistics and p-values for SNR, SNR gain, SCR, and SCR gain, respectively, were as follows: $F_{1,48}$ = 47.45, p = 1.089e-8; $F_{1,48}$ = 124.76, p = 5.995e-15; $F_{1,48}$ = 0.6445, p = 0.4260; $F_{1,48}$ = 0.0414, p = 0.8396. In summary, SNR gains of nearly 18 dB without a significant change in SCR is a substantial improvement in image quality for *in vivo* transcranial ultrasound imaging.

Finally, Fig. 9 shows an example of *in vivo* transcranial B-Mode and DWSA power Doppler imaging with and without 65 bit coded excitation at 6 V. Qualitatively, it is evident that coded excitation reduces the noise floor of the image, thereby improving the separability of blood and noise and increasing blood flow visibility as evidenced by the CNR and CR gains shown in Fig. 9. Note that both power Doppler images in Fig. 9 c and d have been rescaled to the same 40 dB dynamic range for display purposes. Although two of the subjects had good enough acoustic windows to visualize blood flow at 6 V, the other subject did not, so we used the 21 V data for calculating CNR and CR gains. For the 13 bit, 39 bit, and 65 bit codes we measured CNR gains of 2.10 ± 0.30 dB, 4.10 ± 1.00 dB, and 7.25 ± 1.61 dB, respectively and we measured CR gains

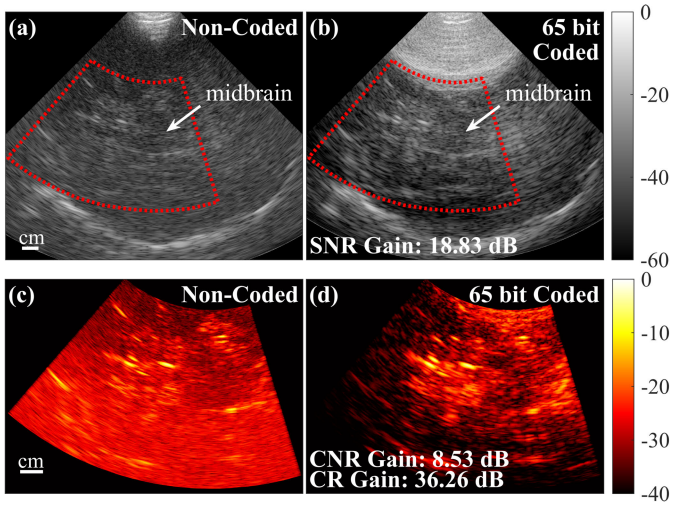

Fig. 9. *In vivo* transcranial power Doppler imaging with and without coded excitation. **(a)** Non-coded B-Mode. **(b)** 65 bit coded B-Mode. For **(a)** and **(b)**, the red box indicates the region for power Doppler processing in **(c)** and **(d)**. The midbrain which is surrounded by blood vessels is indicated. **(c)** Non-coded power Doppler. **(d)** 65 bit coded power Doppler.

of 10.61 ± 0.98 dB, 15.83 ± 6.18 dB, and 27.32 ± 8.08 dB, respectively. The SNR gains for these subjects were 12.59 ± 0.22 dB, 14.98 ± 0.80 dB, and 17.77 ± 1.05 dB which we note are similar to the averages from the ten person study. These results confirm that the SNR gain from coded excitation leads to an increase in blood flow visibility.

V. Discussion

In Section IV-B, we showed in a phantom that an SNR gain of almost 25 dB can be achieved with a 65 bit code. We also showed that the number of transmit elements and the transmit voltage have a large impact on image quality, although this is system dependent. With the system in this study, SNR is maximized with a long code, a high transmit voltage, and about half of the transmit elements. However, SCR begins to drop at such high voltages, presenting an image quality tradeoff. We further analyzed this tradeoff in Section IV-C where we showed that for a given code length and number of transmit elements there is a voltage sweet spot that maximizes SNR and SCR and beyond which they decline.

The results in Sections IV-B and IV-C also demonstrate that using fewer transmit elements can lead to improvements in SNR and SCR with coded excitation using the system in this study. This represents another image quality tradeoff because a large effective transmit aperture is needed to maintain lateral resolution. To address this, synthetic aperture approaches that use fewer transmit elements at a time could be used instead.

The third tradeoff is the limited visibility in the nearfield from transmitting and receiving at the same time. However, in general, coded excitation with extremely long codes is less necessary for such shallow imaging. Placing a stand-off pad between the transducer and imaging target or using different transducers for transmit and receive would also solve this. For example, a dual-transducer system for simultaneously transmitting and receiving long orthogonal codes has been demonstrated before [32].

The phantom experiments demonstrate the flexibility of this coded excitation framework; imaging parameters such as code length, number of transmit elements, and transmit voltage can be adjusted to maximize image quality within the requirements of a specific application. It is important to note that the exact imaging parameters presented here should not be taken out of context and applied to other systems because exact results may differ. Rather, these results should be taken as trends to keep in mind when applying this framework more broadly. When using codes approximately 35 bits or longer or using transducers with more elements than the 64-element P4-2v transducer used here, phantom testing would be advisable.

Another parameter to consider that impacts SNR gain is the bandwidth of the transducer. Many commercially available transducers have a limited bandwidth, including the P4-2v transducer used here which has a fractional bandwidth of 64.4%. The length of the encoding chip pulse could be increased (*e.g.*, from one cycle to two cycles) to reduce the bandwidth of the transmitted coded excitation waveform, ensuring it is well-matched to the transducer bandwidth to maximize transmission efficiency. The improved efficiency increases SNR gain, even when accounting for the longer pulse length [27]. However, the tradeoff is an increased thermal dose for a given code length, limiting the maximum code length that can be safely used. We also found with our system that the two-cycle chip did not compress well with longer codes, leading to a dramatic increase in clutter that outweighed the benefit in SNR gain. In summary, the number of cycles to use for the encoding chip is system- and application-dependent and should be explored along with other imaging sequence parameters to design the best framework.

The decoding chip is another design parameter that should be given some consideration. We ultimately chose to use a decoding chip acquired from Verasonics Simulate Mode which is an approximation of the two-way impulse response of the system on the basis that it provided higher SNR gains and lower range lobe levels than the other decoding chips we tested. However, it is entirely possible that a well-designed setup with a perfect reflector could yield a more accurate two-way impulse response that would further improve decoding. The disadvantage of this approach is that it can be challenging and time consuming to setup such an experiment that requires a well-defined propagation geometry and a highly reflective material that does not produce severe ring-down artifacts as wire targets often do. In addition, we observed small improvements in decoding when we used a simulated impulse response acquired at the same transmit frequency as the data, suggesting that it would be wise to acquire impulse response measurements at multiple frequencies up front. If a new impulse response measurement is required in the future, then a simulation is more reproducible. Also, it is worth noting that SNR gain and range lobe levels may not be the top priority for some applications and other decoding chips may therefore be more optimal. For instance, the delta function decoding chip improved resolution at the cost of lower SNR gains and higher range lobes which may be desirable in some cases.

We also demonstrated *in vivo* translation of this coded excitation framework in thirteen adult volunteers from various demographics. Since age, sex, and race are known to impact bone density and thickness and therefore acoustic window

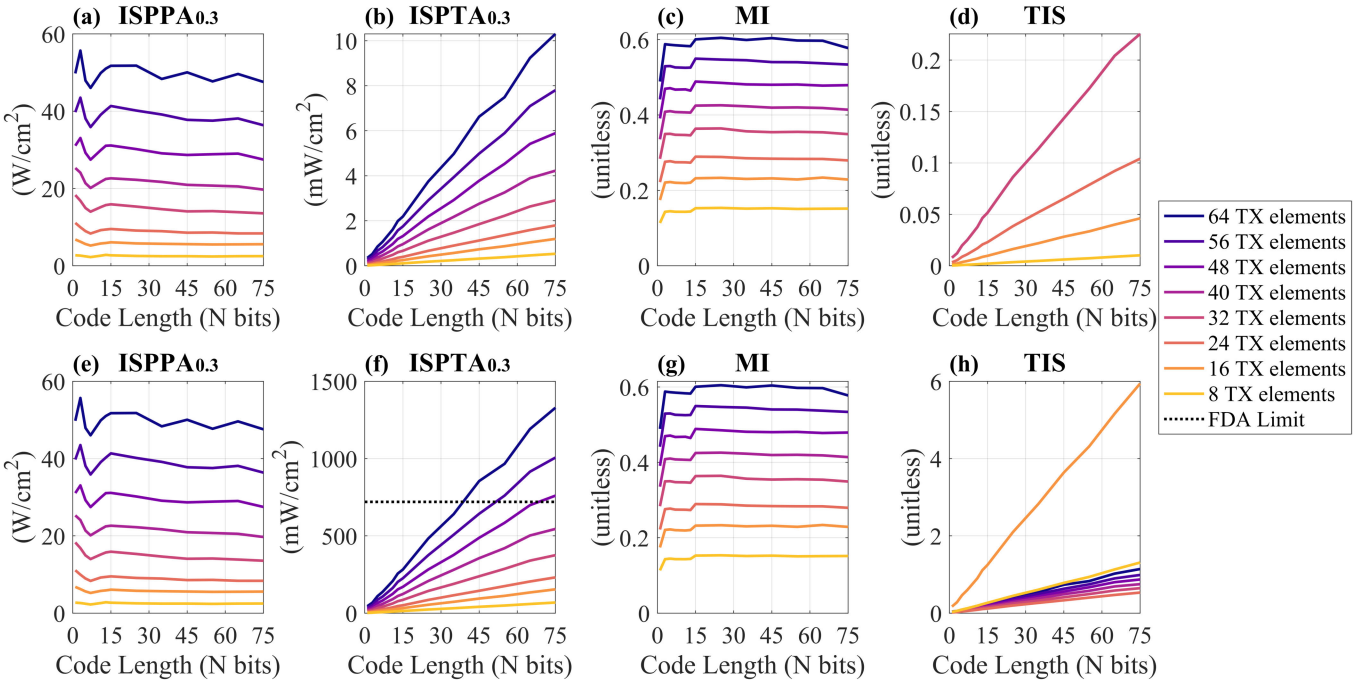

Fig. 10. Acoustic output metrics for Phantom Experiment 1 (Table I). Only data for the 41 V transmit voltage is shown. Panels **(a)** and **(e)** show the derated spatial-peak pulse-average intensity ($ISPPA_{0.3}$), panels **(b)** and **(f)** show the derated spatial-peak temporal-average intensity ($ISPTA_{0.3}$), panels **(c)** and **(g)** shown the mechanical index (MI), and panels **(d)** and **(h)** show the soft tissue thermal index (TIS). Panels **(a)**-**(d)** were computed with an SRF of 7.75 Hz corresponding to the B-Mode pulse sequence and panels **(e)**-**(h)** were computed with a PRF of 1 kHz corresponding to the M-Mode pulse sequence. Note that the SRF or PRF only affects the $ISPTA_{0.3}$ and TIS calculations. The dotted black line in panel **(f)** indicates the FDA Track 1 limit for adult transcranial doppler imaging which is 720 mW/cm^2.

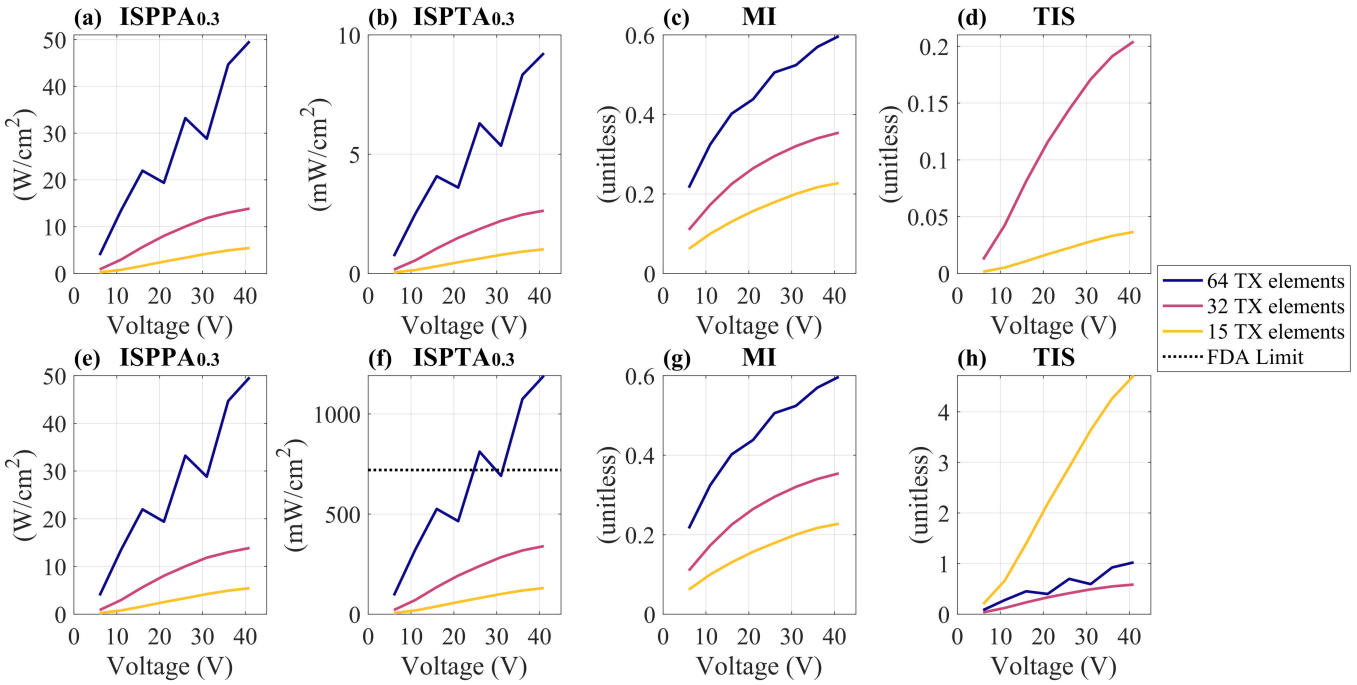

Fig. 11. Acoustic output metrics for Phantom Experiment 2 (Table II). Only data for the 65 bit code is shown. Panels **(a)** and **(e)** show the derated spatial-peak pulse-average intensity ($ISPPA_{0.3}$), panels **(b)** and **(f)** show the derated spatial-peak temporal-average intensity ($ISPTA_{0.3}$), panels **(c)** and **(g)** shown the mechanical index (MI), and panels **(d)** and **(h)** show the soft tissue thermal index (TIS). Panels **(a)**-**(d)** were computed with an SRF of 7.75 Hz corresponding to the B-Mode pulse sequence and panels **(e)**-**(h)** were computed with a PRF of 1 kHz corresponding to the M-Mode pulse sequence. Note that the SRF or PRF only affects the $ISPTA_{0.3}$ and TIS calculations. The dotted black line in panel **(f)** indicates the FDA Track 1 limit for adult transcranial doppler imaging which is 720 mW/cm^2.

suitability, imaging a diverse group is important [1], [2], [3], [4], [33]. We found that our impressions of "good" versus "bad" acoustic windows as well as the SNR and SCR measurements did have a tendency to align with previously

reported demographic trends. By "good" acoustic window, we mean that the window was relatively large and easy to find and the image quality was sufficient to allow quick visualization of the target structure, the midbrain. A "bad" acoustic window in comparison was more challenging to locate and provided poorer visualization of the target structure. Moreover, we saw that SNR gains tended to be larger for the more difficult-to-image subjects, suggesting that coded excitation could help overcome the issue of "failed" acoustic windows that are prevalent in transcranial Doppler exams [3], [4], [5]. We were also able to achieve SNR gains over 18 dB *in vivo* in spite of nonlinear image degradation from the skull. The small SNR gain standard deviations (on the order of 1 dB) further suggest that this coded excitation framework is robust.

The large SNR gains from coded excitation also translate to improved sensitivity in blood flow imaging. Coded excitation both reduces the noise floor and increases the blood flow signal, leading to better separation between blood and noise which can improve the performance of filtering methods such as SVD or ICA that aim to remove the noise component of the signal [29], [34], [35]. This also leads to improved visibility of blood flow which is evidenced by increases in CNR and CR. Moving forward, this sensitivity improvement may enable noninvasive transcranial functional ultrasound neuroimaging.

VI. Conclusion

We presented a coded excitation framework to generate large SNR gains in transcranial ultrasound imaging. We showed how imaging sequence parameters could be optimized to maximize image quality. We also applied our coded excitation framework in transcranial B-Mode and power Doppler imaging and showed large improvements in SNR and blood flow contrast. These improvements may enable transcranial functional ultrasound neuroimaging in the future. The flexibility of this framework along with its compatibility with commonly used scanners make it ideal for broad use.

Appendix A
Acoustic Output Measurements

In this Appendix, we report acoustic output measurements for each sequence and parameter combination used herein to demonstrate the safety of our coded excitation framework and to make this work more generalizable and useful to a broader audience. We conducted these acoustic output measurements in a water tank with a membrane hydrophone according to the guidelines set forth by the FDA and the AIUM/NEMA [28], [36]. The acoustic output metrics we considered were the derated spatial-peak pulse-average intensity ($ISPPA_{0.3}$), the derated spatial-peak temporal-average intensity ($ISPTA_{0.3}$), the derated peak negative pressure ($PNP_{0.3}$), the mechanical index (MI), the soft tissue thermal index (TIS), the bone at focus thermal index (TIB), and the cranial bone at surface thermal index (TIC). TIS and TIB were calculated using the autoscanning equation for the B-Mode and DWSA sequences and the nonscanning equation for the M-Mode sequence [37], [38], [39], [40]. According to the FDA Track 1 limitations for adult transcranial Doppler imaging, the $ISPPA_{0.3}$, $ISPTA_{0.3}$, and MI limits are 190 W/cm^2, 720 mW/cm^2, and 1.9, respectively [28].

TABLE III
Acoustic Output for DWSA Sequence

Code (bits)	$ISPPA_{0.3}$ (W/cm^2)	$ISPTA_{0.3}$ (mW/cm^2)	$PNP_{0.3}$ (MPa)	MI	TIS	TIB	TIC
1	0.66	0.62	0.12	0.07	0.01	0.01	0.02
13	0.94	5.64	0.20	0.12	0.05	0.05	0.22
25	0.68	10.68	0.20	0.12	0.10	0.10	0.42
39	0.70	16.61	0.20	0.12	0.15	0.15	0.65
65	0.70	28.55	0.20	0.12	0.26	0.26	1.12

TABLE IV
Acoustic Output for B-Mode Sequence

Code (bits)	$ISPPA_{0.3}$ (W/cm^2)	$ISPTA_{0.3}$ (mW/cm^2)	$PNP_{0.3}$ (MPa)	MI	TIS	TIB	TIC
1	2.90	0.02	0.25	0.15	0.00	0.00	0.00
13	11.43	0.43	0.45	0.27	0.01	0.01	0.10
25	10.93	0.80	0.47	0.29	0.03	0.03	0.18
39	10.87	1.21	0.47	0.29	0.04	0.04	0.28
65	10.86	2.02	0.48	0.29	0.07	0.07	0.46

TABLE V
Acoustic Output for M-Mode Sequence

Code (bits)	$ISPPA_{0.3}$ (W/cm^2)	$ISPTA_{0.3}$ (mW/cm^2)	$PNP_{0.3}$ (MPa)	MI	TIS	TIB	TIC
1	1.11	0.69	0.12	0.07	0.04	0.01	0.16
13	1.24	5.32	0.16	0.10	0.28	0.07	1.21
25	1.11	10.18	0.17	0.10	0.53	0.13	2.32
39	1.11	15.36	0.17	0.10	0.81	0.20	3.51
65	1.06	25.32	0.17	0.10	1.33	0.34	5.78

We measured the acoustic output for each imaging sequence (B-Mode, M-Mode, DWSA), focal depth (8 cm and 10 cm), code length, number of transmit elements, and transmit voltage. Not all parameter combinations are shown for brevity, but all data is available in an Excel file in the supplementary materials. Fig. 10 shows the $ISPPA_{0.3}$, $ISPTA_{0.3}$, MI, and TIS as a function of code length and number of transmit elements at 41 V and an 8 cm measurement depth for the B-Mode sequence (scan repetition frequency (SRF) = 7.75 Hz, autoscanning mode) and the M-Mode sequence (PRF = 1 kHz, nonscanning mode), corresponding to Phantom Experiment 1 (Table I). Fig. 11 shows the same metrics as a function of voltage and number of transmit elements for the 65 bit code, 8 cm measurement depth, and both the B-Mode and the M-Mode sequences, corresponding to Phantom Experiment 2 (Table II).

Acoustic output measurements are shown for each sequence and code length used *in vivo* in this study in Tables III, IV, and V. These measurements are shown for a 21 V transmit voltage which was the maximum used *in vivo*. For the focused sequences (Tables IV and V), the measurement depth was 10 cm. For the DWSA sequence (Table III), the measurement depth was 3 cm. The DWSA and M-Mode sequences used 15 active transmit elements and the B-Mode sequence used 64 active transmit elements. The M-Mode sequence lasted one second and the DWSA sequence lasted two seconds. The $ISPPA_{0.3}$, $ISPTA_{0.3}$, and MI were all well below the FDA Track 1 limitations.

Acknowledgment

The authors acknowledge Vanderbilt University's Advanced Computing Center for Research and Education (ACCRE), Nick Bottenus, John Flynn, Ying-Chun Pan, Abbie Weeks, Elisa Holtzman, and Adrian Jarquin-Valdivia.

REFERENCES

[1] A. D. Wijnhoud, M. Franckena, A. van der Lugt, P. J. Koudstaal, and E. D. W. J. Dippel, "Inadequate acoustical temporal bone window in patients with a transient ischemic attack or minor stroke: Role of skull thickness and bone density," *Ultrasound Med. Biol.*, vol. 34, no. 6, pp. 923–929, Jun. 2008.

[2] J. Kollár et al., "Image quality of the temporal bone window examined by transcranial Doppler sonography and correlation with postmortem computed tomography measurements," *Cerebrovascular Diseases*, vol. 17, no. 1, pp. 61–65, 2004.

[3] A. A. Jarquin-Valdivia, J. McCartney, D. Palestrant, S. C. Johnston, and D. Gress, "The thickness of the temporal squama and its implication for transcranial sonography," *J. Neuroimag.*, vol. 14, no. 2, pp. 139–142, Apr. 2004.

[4] A. W. J. Hoksbergen, D. A. Legemate, D. T. Ubbink, and M. J. H. M. Jacobs, "Success rate of transcranial color-coded duplex ultrasonography in visualizing the basal cerebral arteries in vascular patients over 60 years of age," *Stroke*, vol. 30, no. 7, pp. 1450–1455, Jul. 1999.

[5] T. Postert, J. Federlein, H. Przuntek, and T. Büttner, "Insufficient and absent acoustic temporal bone window: Potential and limitations of transcranial contrast-enhanced color-coded sonography and contrast-enhanced power-based sonography," *Ultrasound Med. Biol.*, vol. 23, no. 6, pp. 857–862, Jan. 1997.

[6] G. Pinton, J.-F. Aubry, E. Bossy, M. Müller, M. Pernot, and M. Tanter, "Attenuation, scattering, and absorption of ultrasound in the skull bone," *Med. Phys.*, vol. 39, pp. 299–307, Jan. 2012.

[7] S. Pichardo, V. W. Sin, and K. Hynynen, "Multi-frequency characterization of the speed of sound and attenuation coefficient for longitudinal transmission of freshly excised human skulls," *Phys. Med. Biol.*, vol. 56, no. 1, pp. 219–250, Jan. 2011.

[8] K. K. Shung, R. A. Sigelmann, and J. M. Reid, "Scattering of ultrasound by blood," *IEEE Trans. Biomed. Eng.*, vol. BME-23, no. 6, pp. 460–467, Nov. 1976.

[9] S. Bjærum, H. Torp, and K. Kristoffersen, "Clutter filter design for ultrasound color flow imaging," *IEEE Trans. Ultrason., Ferroelectr., Freq. Control*, vol. 49, no. 2, pp. 204–216, Feb. 2002.

[10] A. Heimdal and H. Torp, "Ultrasound Doppler measurements of low velocity blood flow: Limitations due to clutter signals from vibrating muscles," *IEEE Trans. Ultrason., Ferroelectr., Freq. Control*, vol. 44, no. 4, pp. 873–881, Jul. 1997.

[11] L. Lindvere et al., "Cerebral microvascular network geometry changes in response to functional stimulation," *NeuroImage*, vol. 71, pp. 248–259, May 2013.

[12] C. Demené et al., "Transcranial ultrafast ultrasound localization microscopy of brain vasculature in patients," *Nature Biomed. Eng.*, vol. 5, no. 3, pp. 219–228, Mar. 2021.

[13] R. Y. Chiao and X. Hao, "Coded excitation for diagnostic ultrasound: A system developer's perspective," *IEEE Trans. Ultrason., Ferroelectr., Freq. Control*, vol. 52, no. 2, pp. 160–170, Feb. 2005.

[14] T. Misaridis and J. A. Jensen, "Use of modulated excitation signals in medical ultrasound. Part I: Basic concepts and expected benefits," *IEEE Trans. Ultrason., Ferroelectr., Freq. Control*, vol. 52, no. 2, pp. 177–191, Feb. 2005.

[15] T. Misaridis and J. A. Jensen, "Use of modulated excitation signals in medical ultrasound. Part II: Design and performance for medical imaging applications," *IEEE Trans. Ultrason., Ferroelectr., Freq. Control*, vol. 52, no. 2, pp. 192–207, Feb. 2005.

[16] M. O'Donnell, "Coded excitation system for improving the penetration of real-time phased-array imaging systems," *IEEE Trans. Ultrason., Ferroelectr., Freq. Control*, vol. 39, no. 3, pp. 341–351, May 1992.

[17] H. Zhao, L. Y. L. Mo, and S. Gao, "Barker-coded ultrasound color flow imaging: Theoretical and practical design considerations," *IEEE Trans. Ultrason., Ferroelectr., Freq. Control*, vol. 54, no. 2, pp. 319–331, Feb. 2007.

[18] Y. Wang, K. Metzger, D. N. Stephens, G. Williams, S. Brownlie, and M. O'Donnell, "Coded excitation with spectrum inversion (CEXSI) for ultrasound array imaging," *IEEE Trans. Ultrason., Ferroelectr., Freq. Control*, vol. 50, no. 7, pp. 805–823, Jul. 2003.

[19] J. Udesen, F. Gran, K. L. Hansen, J. A. Jensen, C. Thomsen, and M. B. Nielsen, "High frame-rate blood vector velocity imaging using plane waves: Simulations and preliminary experiments," *IEEE Trans. Ultrason., Ferroelectr., Freq. Control*, vol. 55, no. 8, pp. 1729–1743, Aug. 2008.

[20] F. Gran, J. Udesen, M. B. Nielsen, and J. A. Jensen, "Coded ultrasound for blood flow estimation using subband processing," *IEEE Trans. Ultrason., Ferroelectr., Freq. Control*, vol. 55, no. 10, pp. 2211–2220, Oct. 2008.

[21] R. C. Daniels and V. Gregers-Hansen, "Code inverse filtering for complete sidelobe removal in binary phase coded pulse compression systems," in *Proc. IEEE Int. Radar Conf.*, May 2005, pp. 256–261.

[22] J. Ruprecht and M. Rupf, "On the search for good aperiodic binary invertible sequences," *IEEE Trans. Inf. Theory*, vol. 42, no. 5, pp. 1604–1612, Sep. 1996.

[23] E. Vienneau and B. Byram, "Compound barker-coded excitation for increased signal-to-noise ratio and penetration depth in transcranial ultrasound imaging," in *Proc. IEEE Int. Ultrason. Symp. (IUS)*, Sep. 2020, pp. 1–4.

[24] E. P. Vienneau and B. C. Byram, "A coded excitation framework for increased signal-to-noise ratio of in vivo ultrasound power Doppler imaging," *Proc. SPIE*, vol. 11602, Feb. 2021, Art. no. 116020P.

[25] E. P. Vienneau and B. C. Byram, "Method and system using coded excitation with invertible skew-symmetric binary sequences and inverse filtering," WO Patent 2022051238 A1, 2021. [Online]. Available: https://patents.google.com/patent/WO2022051238A1/

[26] B. Kiranmai and P. R. Kumar, "Performance evaluation of compound barker codes using cascaded mismatched filter technique," *Int. J. Comput. Appl.*, vol. 121, no. 19, pp. 31–34, Jul. 2015.

[27] A. Nowicki, I. Trots, P. A. Lewin, W. Secomski, and R. Tymkiewicz, "Influence of the ultrasound transducer bandwidth on selection of the complementary Golay bit code length," *Ultrasonics*, vol. 47, no. 1, pp. 64–73, 2007.

[28] *Marketing Clearance of Diagnostic Ultrasound Systems and Transducers: Guidance for Industry and Food and Drug Administration Staff*, U.S. Food & Drug Admin., Silver Spring, MD, USA, 2019.

[29] J. Tierney, K. Walsh, H. Griffith, J. Baker, D. B. Brown, and B. Byram, "Combining slow flow techniques with adaptive demodulation for improved perfusion ultrasound imaging without contrast," *IEEE Trans. Ultrason., Ferroelectr., Freq. Control*, vol. 66, no. 5, pp. 834–848, May 2019.

[30] E. Vienneau, K. Ozgun, and B. Byram, "A Coherence-based technique to separate and quantify sources of image degradation in vivo with application to transcranial imaging," in *Proc. IEEE Int. Ultrason. Symp. (IUS)*, Sep. 2020, pp. 1–4.

[31] E. P. Vienneau, K. A. Ozgun, and B. C. Byram, "Spatiotemporal coherence to quantify sources of image degradation in ultrasonic imaging," *IEEE Trans. Ultrason., Ferroelectr., Freq. Control*, vol. 69, no. 4, pp. 1337–1352, Apr. 2022.

[32] F. Nicolet, E. Carcreff, H. Liebgott, and B. Nicolas, "Synthetic transmit aperture imaging using orthogonal coded sequences with separate transmitters-receivers," in *Proc. IEEE Int. Ultrason. Symp. (IUS)*, Oct. 2022, pp. 1–4.

[33] E. M. Lillie, J. E. Urban, S. K. Lynch, A. A. Weaver, and J. D. Stitzel, "Evaluation of skull cortical thickness changes with age and sex from computed tomography scans," *J. Bone Mineral Res.*, vol. 31, no. 2, pp. 299–307, Feb. 2016.

[34] J. Baranger, B. Arnal, F. Perren, O. Baud, M. Tanter, and C. Demené, "Adaptive spatiotemporal SVD clutter filtering for ultrafast Doppler imaging using similarity of spatial singular vectors," *IEEE Trans. Med. Imag.*, vol. 37, no. 7, pp. 1574–1586, Jul. 2018.

[35] J. Tierney, J. Baker, D. Brown, D. Wilkes, and B. Byram, "Independent component-based spatiotemporal clutter filtering for slow flow ultrasound," *IEEE Trans. Med. Imag.*, vol. 39, no. 5, pp. 1472–1482, May 2020.

[36] *Acoustic Output Measurement Standard for Diagnostic Ultrasound Equipment: Revision 1*, American Institute of Ultrasound in Medicine and National Electrical Manufacturers Association, Rosslyn, VI, USA, 2007.

[37] J. G. Abbott, "Rationale and derivation of MI and TI—A review," *Ultrasound Med. Biol.*, vol. 25, no. 3, pp. 431–441, Mar. 1999.

[38] W. R. Hedrick and D. L. Hykes, "An overview of thermal and mechanical acoustic output indices," *J. Diagnostic Med. Sonography*, vol. 9, no. 5, pp. 228–235, Sep. 1993.

[39] T. A. Bigelow et al., "The thermal index: Its strengths, weaknesses, and proposed improvements," *J. Ultrasound Med.*, vol. 30, no. 5, pp. 714–734, May 2011.

[40] A. Nowicki, "Safety of ultrasonic examinations; thermal and mechanical indices," *Med. Ultrason.*, vol. 22, no. 2, pp. 203–210, May 2020.